Adding geodetic strain rate data to a seismogenic context

A. Caporali

Dipartimento di Geologia, Paleontologia e Geofisica, Università di Padova, Italy

(Received April 18, 2005; accepted June 30, 2005)

ABSTRACT In several seismically active areas deformation processes at depth must generate deformation at the surface, and the measurement of such surface deformation is an important boundary condition for models of the evolution of interacting blocks before, during and after earthquakes. The network of some 160 permanent GPS stations disseminated in Europe under the European Permanent Network of EUREF, with additional densification stations in particular areas such as the north east of Italy, provides a valuable contribution to the estimate of the average surface strain rate. The expected strain rate is of the order of 20-40 nanostrain per year, corresponding to a velocity change of a few mm/year over distances of some hundreds of kilometers. Consequently, we must require accuracy in the velocities of fractions of mm/year, and full control of systematic errors which may mask tectonic signals. The procedures for the systematic processing of SINEX files, representing the densified network, are reviewed here with the intent of meeting and possibly exceeding such specifications. A method for determining the noise in time series of coordinates, and of obtaining a reliable estimate of the accuracy in the estimated station velocities is described. In particular, it is shown that, on average, at least three years of continuous tracking of a permanent GPS station are required for a reliable estimate of its velocity. Then the problem of calculation of the velocity field and its horizontal gradient is addressed. We focus on the algorithm of weighted least squares collocation as a technique of minimum variance to interpolate velocities and strain rates. We present the large scale velocity flow across most of continental Europe, after subtraction of a rigid rotation approximating the generalised NE drift of Eurasia, showing a variety of intraplate and interplate processes. Finally we review the frictional model of Anderson to describe fault interaction and stress release, and present analytical expressions for recurrence times of fault instabilities. This simple framework enables a number of key problems to be identified to make proper use of the geodetically inferred strain rate data. Taking the seismicity in Friuli as a test bed, we discuss requirements on the knowledge of fault geometries, local rheology, fault plane solutions, role of pore fluid pressure and historical seismicity which, in conjunction with the surface geodetic data, are necessary to attempt a more advanced modelling of the dynamic and potentially seismogenic processes at depth.

1. Introduction

Surface deformation at the surface reflects both the plate driving forces acting at the bottom, and stress changes at or near fault areas on the top. Stress is, in most cases, released seismically at pre-existing faults. The slip geometry and the detail of the vertical fault profile are constrained by seismological and structural data, but they are by themselves insufficient to shed light on the

dynamics of an earthquake and, eventually, on the hypothesis of an idealized seismic cycle. Geodetic measurements of strain rate are crucial to reconstruct the deformation pattern of a fault in space and time. The strain rates involved are small, of the order of 10 to 100 nanostrains per year (1 nanostrain = 10^{-9}), but continuous measurements over three or more years of the coordinates of GPS permanent stations seem to have the stability and repeatability to ensure a reliable estimation of such small signals with sufficient accuracy. Of the several areas that are prone to a synergy among geodesy, seismology and structural geology, Friuli is very attractive. Over the past thirty years, after the earthquake of May 1976, field surveys and seismic profiles, particularly CROP (Montrasio and Sciesia, 1994) and Transalp (Transalp Working Group, 2002), have shed new light on the structure of the Central and Eastern Alps. Seismic networks (http://www.crs.inogs.it) have been collecting data continuously, enabling fault plane solutions and seismic moments to be determined for several earthquakes. More recently, a number of permanent GPS stations have been installed to form the precision regional network FredNet (http://www.crs.inogs.it/frednet). Although the time span covered by these stations is unfortunately still too short for a reliable determination of the velocities, it is nevertheless possible to combine these data with data from other stations in Italy, Croatia, Slovenia and Austria and attempt a first map of the strain rate in the area.

The purpose of this paper is twofold. First, the systematic processing of GPS data yielding estimates of velocities and strain rates will be reviewed, with particular attention to the reliability and the spatial resolution of the estimated strain rates. Secondly, using the classical Anderson theory of faulting, we will combine the geodetic information with a simple 'slider block' model of the seismogenic fault of the 1976 earthquake. Using the static and dynamic equations of this idealized model we will address the estimation of a number of important parameters, such as critical deviatoric stress, shear stress drop, energy drop, slip and frictional heating associated with the earthquake, and finally the question of the repeat time of the seismic cycle.

2. The geodetic data

Our approach to local estimates of the strain rate tensor benefits from a highly structured and rigorously maintained network of permanent GPS stations known as EPN (European Permanent Network: http://www.epncb.oma.be) of the EUREF (Fig. 1). The network consists of some 160 stations operating continuously. Data are collected at the Data Center of the Bundesamt fuer Kartographie und Geodaesie (BKG) in Frankfurt on a daily basis (Bruyninx, 2000). A Consortium of 16 Local Analysis Centers (LAC) processes partially overlapping subnetworks of the EPN on a weekly basis, so that each station of the network is analysed by three or more LACs following processing standards that represent the state-of-the-art modelling of the data and estimation algorithms. Finally, the normal equations produced by each LAC for a given week are merged by the BKG into one normal equation system. The network is consequently readjusted and properly aligned to the International Terrestrial Reference System on a weekly basis. Hence, the EPN issues weekly, a normal equation for the entire network in the conventional SINEX format. Such SINEX file is a valuable metadata that includes the adjusted coordinates, their variance covariance matrix, and the constraints which were adopted for the alignment of the net. These constraints are explicitly mentioned and are removable, so that the same SINEX file can

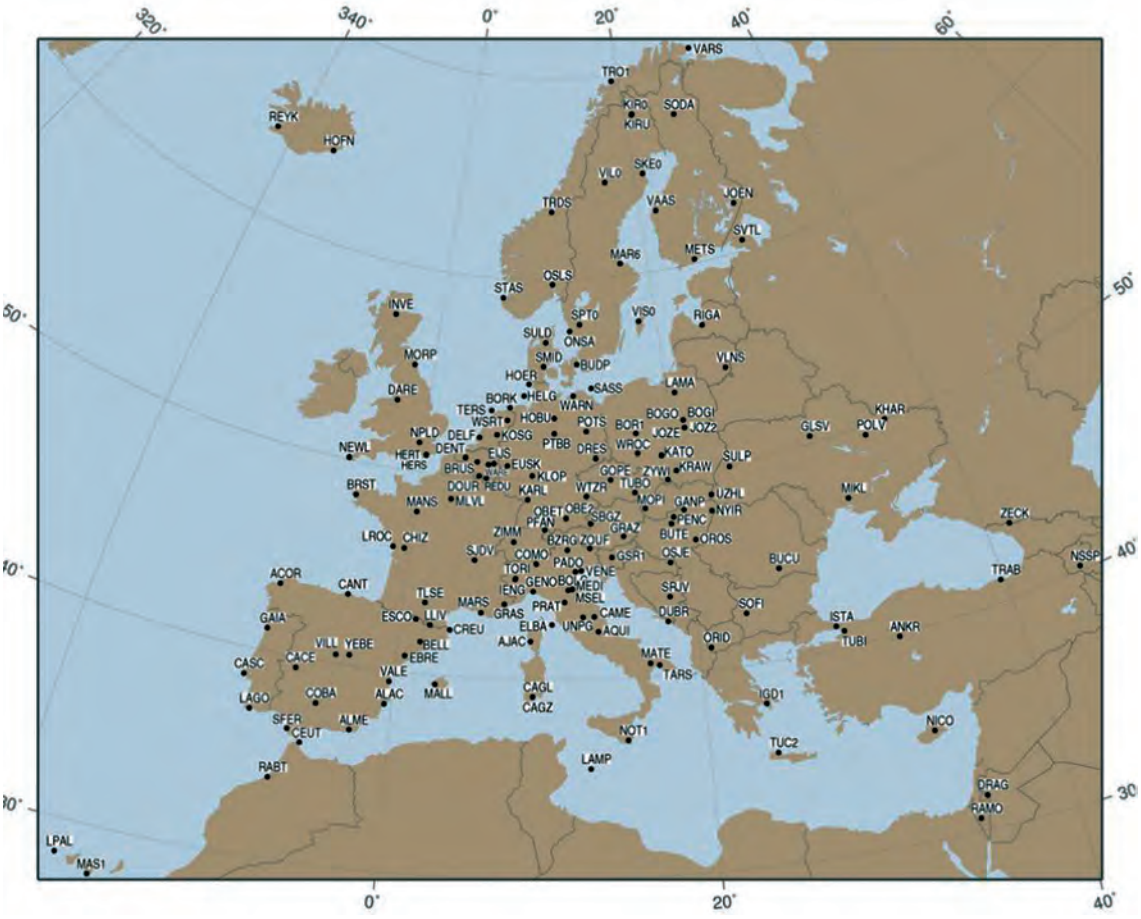

Fig. 1 - The European Permanent Network (EPN) managed by EUREF and consisting of some 160 high quality, permanently operating GPS stations. Data are analysed weekly by 16 Local Analysis Centers, coordinated by one combination center and supervised by a Technical Working Group. Source: http://www.epncb.oma.be .

be re-used with different constraints at any time. Because these standardized SINEX files of the EPN network have been available since GPS week 860 (June 1996), accurate and continuous time series of coordinates could be computed for the EPN, resulting in a quantitative measurement of its deformation history. Unfortunately, the spacing of the GPS stations is conceived for the maintenance of the European geographic reference system, rather than for geodynamical applications. Consequently, it is necessary to intensify the EPN network, to improve its spatial resolution. To this purpose, the Local Analysis Center UPA at the University of Padova has been systematically processing data from a network of Italian and Austrian permanent GPS stations with the same procedures (software, setup and models) as for the EPN work since GPS week 995. The present status of this more dense Italian network is shown in Fig. 2. This parallel processing has resulted in a collection of weekly SINEX files completely compatible with the EPN SINEX files of the corresponding weeks. To locally densify the EPN geodetic network, we have henceforth adopted the approach of combining, on a weekly basis, the EPN SINEX with the

Site	V_x (mm/yr)	V_y (mm/yr)	V_z (mm/yr)
GRAZ	-17.60	17.70	8.30
ZIMM	-13.80	18.50	10.00
VILL	-9.90	20.00	11.10
JOZE	-18.10	16.20	7.40
POTS	-16.10	16.10	7.70
GRAS	-13.10	18.90	10.10

Table 1 - ITRF00 velocities of fiducial sites used to align the network to a conventional Reference Frame.

corresponding UPA SINEX file. The result is an increased SINEX file, for each week. Eventually, the set of EPN SINEX files from week 860 to 994, and the set of increased SINEX files from GPS week 995 to the present (week 1300) were staked, ITRF2000 (http://itrf.ensg.ign.fr/ITRF_solutions/2000/ITRF2000.php) constraints were imposed on the position and velocity at a reference epoch of fiducial stations (see Table 1), and an estimate of mean coordinates and velocities was obtained, together with their covariance matrix.

3. Noise in the time series of coordinates

The time series of the coordinates of the individual stations are the result of the normal equation stacking, using the Bernese 4.2 program (Beutler *et al*., 2001), with the addition of the ITRF2000 constraints to define a conventional datum for position and velocity. After removal of a best-fitting straight line, the time series resemble a random sequence with zero mean and a root mean square (rms) dispersion typically of the order of a few millimetres. Spectral analyses, however, in most cases reveal the presence of an annual signal. Its origin is unlikely to be related to errors in the assumed coordinates of the pole, because in such a case the annual sinusoids at the various sites would be correlated, and the phase lags can be predicted exactly from the nominal geographic position of the stations. A more likely explanation may be the thermal gradients in the monumentation, or periodic fluid migration in the underground. After removing the annual signal by standard least squares, the resulting time series are again spectrally analysed to define the way noise power is distributed in a frequency band which ranges from a low limit (the inverse of the length of the series) to a high limit (the Nyquist frequency is one cycle every two weeks). The one-sided power spectral density $S_x(f)$ of the de-trended time series $x(t)$ can be approximated by a linear combination of power laws $G_x(f)$:

$$S_x(f) \approx G_x(f) = \sum_{i=0}^{4} \frac{h_{-i}}{f^i} \left[mm^2 yr \right] \qquad (1)$$

i = 0 White Phase Noise;
i = 1 Flicker Phase Noise;
i = 2 White Frequency Noise or Random Phase Walk;
i = 3 Flicker Frequency Noise;
i = 4 Random Frequency Walk

Fig. 2 - A densification of the EPN shown in Fig. 1 is realized by means of the contribution of several Public and Private Institutions running permanent GPS stations of the same quality standards as the EPN stations and making their data available for scientific use.

where i is the spectral index. The amplitude of each noise term h_{-i} is estimated by the least squares fit of the model in Eq. (1) to the spectrum $S_x(f)$ of the de-trended, zero-mean time series of the station coordinates.

Caporali (2003) found that for most time series the power spectral density follows a power law, with a spectral index of -1 for frequencies up to 1 cycle every six months, and a spectral index of zero for higher frequencies. Hence, the noise profile is a flicker phase noise (or f^{-1}) at low frequencies and a white phase noise (or f^{0}) at higher frequencies. The presence of significant coloured noise in the low-frequency band has an impact on the estimate of the uncertainty of the regression parameters, and, notably the slope, of the straight line which is normally computed to interpolate the time series. Were the noise white at all frequencies, then the formal uncertainty computed by the standard least squares would be a reliable estimate of the true uncertainty. The presence of different power laws in different frequency bands requires a different approach than for the standard formal error, to estimate the uncertainty in the slope, and hence in the velocity. A time domain description of the uncertainty in the slope of a time series $x(t)$ is the sample variance of fractional frequency variations. The average velocity over an interval T at time t_k is

$$\bar{y}_k = \frac{x(t_k + T) - x(t_k)}{T}, \tag{2}$$

where k=1,2,… is the sample number. When N consecutive samples are measured, each of duration T, the variance of the ensemble is known as the Allan variance (Allan, 1966):

$$\left\langle \sigma_y^2(N,T) \right\rangle \equiv \left\langle \frac{1}{N-1} \sum_{n=1}^{N} \left(\bar{y}_n - \frac{1}{N} \sum_{k=1}^{N} \bar{y}_k \right)^2 \right\rangle, \tag{3}$$

where the brackets denote infinite time average. The Allan variance, in the time domain, represents a definition of stability in the rate of change of the time series, in the sense of probability of change in slope. Because of the existence of processes causing this variance to diverge for a large N, Allan (1966) suggested the introduction of the two sample (i.e. N=2) variance:

$$\sigma_{\mathrm{T}}^2 \equiv \left\langle \sigma_{\mathrm{T}}^2(2,T) \right\rangle = \frac{1}{2} \left\langle \left(\bar{y}_{k+1} - \bar{y}_k \right)^2 \right\rangle, \tag{4}$$

This is the variance factor of the probability of a change in rate [Eq. (2)] from one portion of the time series to the next consecutive, both being of length T.

The one - sided spectrum of a time series of coordinates $S_x(f)$ is related to that of the rate of change $S_y(f)$ of the time series by the equation $S_y(f)=(2pf)^2 S_x(f)$. The relation between the two-sample Allan variance and the spectral density $S_x(f)$ of the time series is obtained assuming a stationary process (i.e. the time average of the ensemble is not affected by a time translation) and that $\langle y_k \rangle^2 = 0$ (i.e. we are considering departures from the average rate of change):

$$\sigma_{\mathrm{T}}^2 = \frac{1}{T^2} E\left[x(T) - x(0) \right]^2 = \frac{2}{T^2} \left[R_x(0) - R_x(T) \right]. \tag{5}$$

$E[]$ denotes the expectation value. Hence, the variance of the average rate of change depends on

the autocorrelation $R_x()$ of the coordinate jitter $x(t)$. Using the Wiener - Khinchin Fourier Transform relationship between the one - sided spectral density of a random signal and its autocorrelation function $(\omega=2\pi f)$:

$$R_x(T)=\frac{1}{\pi}\int_0^{\infty}S_x(\omega)\cos(\omega T)d\omega \tag{6}$$

we finally obtain the expression of the two-sample Allan variance of a time series with spectrum S_x, as a function of the time T:

$$\sigma_\tau^2=\frac{2}{\pi T^2}\int_0^{\infty}S_x(\omega)(1-\cos\omega T)d\omega=\frac{1}{\pi}\int_0^{\infty}S_y(\omega)\frac{\sin^2\frac{\omega T}{2}}{\left(\frac{\omega T}{2}\right)}d\omega \tag{7}$$

The Allan variance is an estimate of the stability of a time series, in the sense of maximum change in slope which can take place with 1 σ probability between two consecutive, non-overlapping and equal-length batches of data. The Allan variance is normally computed as a function of the length of the batch. Taking, for example, a time series of five years, it is of valuable interest to estimate the maximum change in slope expected in the next five years. In the event of a larger change than that corresponding to the Allan variance, some form of signal, for example geodynamic or other, should be considered as a cause. Contrary to the formal error computed by least squares, which assumes white noise at all frequencies, the Allan variance [(Eq. (7)] embodies the full spectral structure of the noise of a series, and is therefore capable of embodying the property of our time series: i.e. flicker phase noise prevails at low frequencies while white noise dominates higher frequencies.

Coloured noise in a time series affects not only the estimated uncertainty of the slope but also the nominal value of the slope, relative to the values that would be obtained by standard least squares. We consider a simple linear regression:

$$X_0=AZ+\varepsilon(t) \tag{8}$$

where X_0 is the time-series of the coordinates, A is the partial derivative matrix of the linear regression, Z is the two-dimensional vector of the unknown intercept and velocity, and $\varepsilon(t)$ is the noise vector with elements $x(t)$.

If the power spectral density of the time series follows a power law with a non zero spectral index, then the corresponding autocorrelation function should differ from a Dirac delta in the time domain. This means that the coordinates at a given epoch are statistically dependent from coordinates at different epochs. Because one normally assumes uncorrelated samples in standard least squares, i.e. diagonal weight matrix of the input data, then the estimated slope and intercept could in principle be affected by the non diagonality of the weight matrix. More specifically, all the samples are assumed with the same variance and approximate their covariance with the normalized autocorrelation $\rho_x(T)=R_x(T)/R_x(0)$, T being the lag between any two data points. By standard least squares formulae:

$$Z \equiv \begin{bmatrix} x_0 \\ v_0 \end{bmatrix} = \left[A^T \rho_x A \right]^{-1} A^T \rho_x X_0 \tag{9}$$

and the variance of the velocity is related to the variance of the time series σ_0^2 by the (2,2) element of the variance covariance matrix of the linear regression (the (1,1) element is the variance of the intercept) in Eq. (9):

$$\sigma^2_{V_0} = \left| \left[A^T \rho_x A \right]^{-1} \right|_{22} \sigma_0^2 \tag{10}$$

The effect of the data being autocorrelated on the slope estimate has been tested (Caporali, 2003) in a number of time series of EPN permanent stations with three or more years of continuous tracking. It turns out that the effect is negligibly small for virtually all stations examined, basically because the decorrelation time is of the order of a few weeks, which is short compared to the length of the time series.

In conclusion, the estimates of the velocities remain unchanged whether or not the non diagonality of the correlation matrix is taken into account, but the formal uncertainties in the velocities are smaller by a factor of ~ 4 relative to the stability of the time series, as defined by the Allan variance. This rescaling is a consequence of the 1/f 'flicker phase' noise in the time series at low frequencies. However, the cause of this particular noise remains unclear at present.

Fig. 3 shows an example of the time series of the permanent station PADO: the time series for each coordinate are shown in Fig. 3a; the identification of periodicities, in particular the annual term, is shown in Fig. 3b in the time (left) and frequency (right) domain; the spectral properties of the time series after removal of long periodic terms are shown on the left-hand side of Fig. 3c, with an estimate of the spectral index. On the right-hand side, we plot the autocorrelation function. Finally, Fig. 3d shows the Allan variance of each series, as an indication of the time stability of the time series. Similar plots for the other European stations are available at the web site http://cisas.unipd.it/gps/project.html.

4. From scattered velocities to a velocity field and its horizontal gradient

The velocities at the GPS sites, and their uncertainties, form the basis to estimate the tectonic flow of a surface, and its horizontal gradient, namely the strain rate tensor (Caporali *et al*., 2003). For this purpose, we require an interpolation algorithm that maps the scattered data to a regular grid. In the literature, two different approaches are proposed. One is based on the Delaunay triangulation, where triangles with vertexes are formed at the stations, and linear interpolation is used to map the data to the nearest grid point. This is the simplest method to implement and works very well under the assumptions of very regular spacing of the stations, and homogeneous values of their uncertainties, which is unfortunately only rarely the case. Velocities of stations with just three years of data (the minimum required to estimate velocities) are analysed together with those of stations with eight years of data. Some stations are clustered, while there exist elsewhere relatively large areas with a comparatively smaller population of stations. An additional

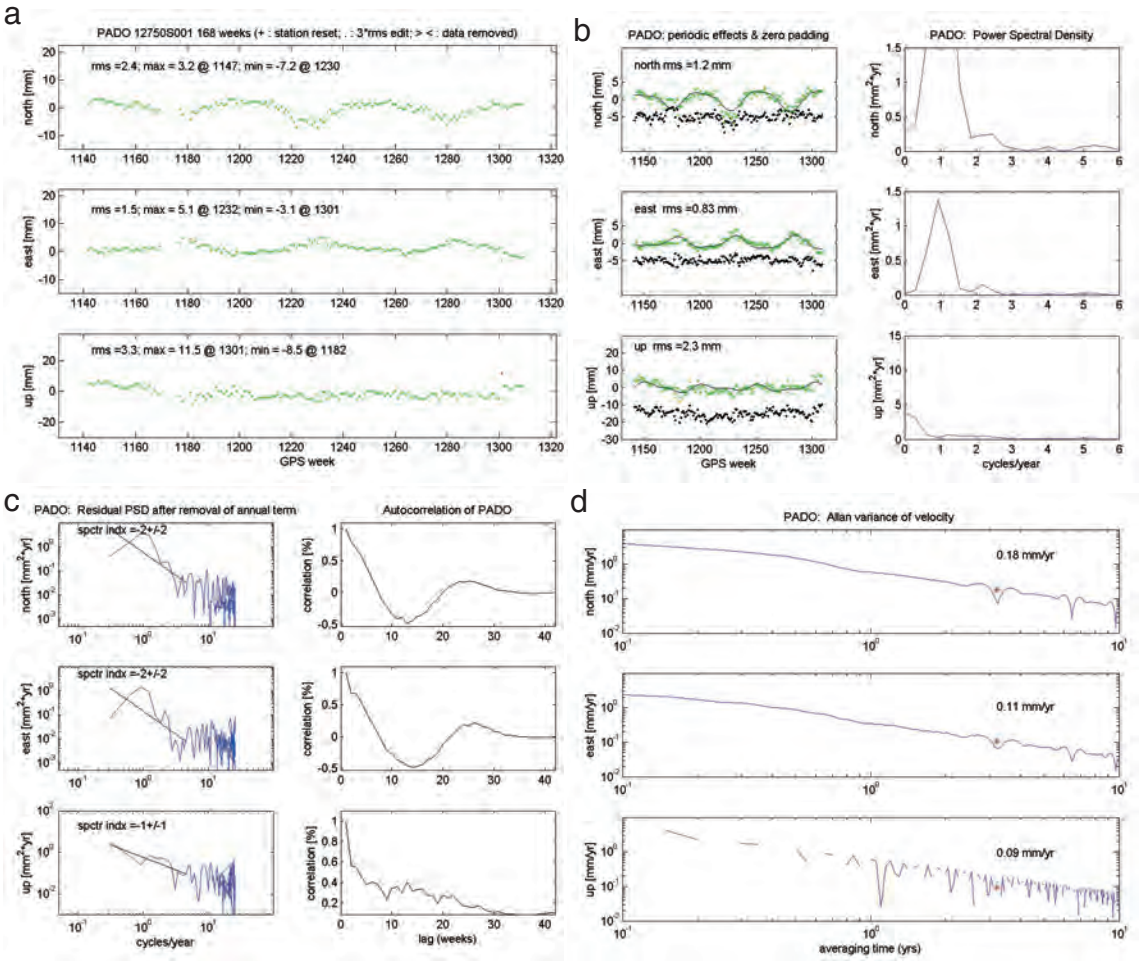

Fig. 3 - Example of the analysis of time series of coordinates of the permanent station PADO. The time series for each coordinate are shown in Fig. 3a; the identification of periodicities, in particular the annual term, is shown in Fig. 3b in the time (left) and frequency (right) domain; the spectral properties of the time series after removal of long periodic terms are shown in the left hand side of Fig. 3c, with an estimate of the spectral index. On the right hand side, we plot the autocorrelation function. Finally, Fig. 3d shows the Allan variance of each series, as an indication of the time stability of the time series. The velocities given in this figure represent the maximum velocity change which can be expected with 1σ confidence in the next 168 weeks.

complication in the Delaunay approach is related to the estimate of the horizontal velocity gradient and its uncertainty: it is unclear how to propagate the covariance of the velocity of a permanent station to a covariance of the strain rate tensor. A second approach, based on least squares collocation, seems more suited to cope with the geographical and statistical properties of our input scattered velocities, although at the expenses of a larger computation time. Least squares collocation requires a covariance function for the data to be specified. This function defines how the input data decorrelate with increasing lag distance. Although there is no other constraint that its regularity at the origin (it should be finite at zero lag and have zero derivative) and at infinity (it should tend to zero), the choice of the function is arbitrary. A popular selection

is the isotropic covariance function, falling off to infinity as the inverse square of the lag distance d:

$$C_{ij}(d)=\frac{C_{ij}(0)}{1+(d/d_0)^2}\;\; i,j=e(ast),n(orth);\; C(d)=\begin{bmatrix} C_{nn} & C_{en} \\ C_{en} & C_{ee} \end{bmatrix} \tag{11}$$

The non-diagonal structure of the matrix C implies that, for example, to compute the north component of the velocity at a grid point we consider not only the contribution of the north velocities at all the data points through the matrix C_{nn}, but also the contribution of the east velocities through the matrix C_{en}.

The covariance matrix C depends on a scale distance d_0, which should be determined by the data themselves. Other choices are also possible, and the final result is, to a large extent, independent of the form of the function. Least squares collocation is a minimum variance algorithm which interpolates the velocity at a grid point by means of a weighted sum of the velocities at all the data points, with a weight dependent on the distance of the grid point from the individual data points. If the input velocities have uneven uncertainties, then the covariance function can be conveniently complemented with the a priori covariance W of the input velocities. In this manner, one takes into account proper the a priori statistics of the input data:

$$\begin{bmatrix} v_n \\ v_e \end{bmatrix}_p = \sum_s C(d_{P,s}) \sum_{s'} \left[C(d_{s,s'}) \right]^{-1} \cdot \begin{bmatrix} v_n \\ v_e \end{bmatrix}_{s'} \quad s,s' = station\ indeces \tag{12}$$

with

$$W=\frac{\frac{1}{\sigma^2}}{\sum\frac{1}{\sigma^2}} \tag{13}$$

and σ^2 is, for example, the Allan variance of each velocity.

The computational effort required by this method is that it requires the inversion of a squared matrix of dimension equal to the number of available data points. However, this inversion is required only once. The covariance of the interpolated velocity is obtained by taking the ensemble average of the product of the transposed interpolated velocity times the interpolated velocity:

$$\begin{bmatrix} \sigma_{nn}^2 & \sigma_{ne} \\ \sigma_{ne} & \sigma_{ee}^2 \end{bmatrix} = \sum_{s,s',s'',s'''} C(d_{P,s}) \cdot \left[C(d_{s'',s'''}) + W_{s''s'''} \right]^{-1} C^T(d_{P,s'''}) \quad s,s',s'',s''' = station\ indices \tag{14}$$

The matrix S in Eq. (14) represents the covariance of the scattered velocities, and is found in the SINEX file resulting from the normal stacking equation yielding the time series.

The eigenvalues of the covariance matrix of the velocity (14) yield the error ellipse of the interpolated velocity at every grid point P. The collocation assumes that the input data have zero mean. Hence, after interpolation the mean value will have to be added back.

The components of the strain-rate tensor are obtained likewise by considering the horizontal

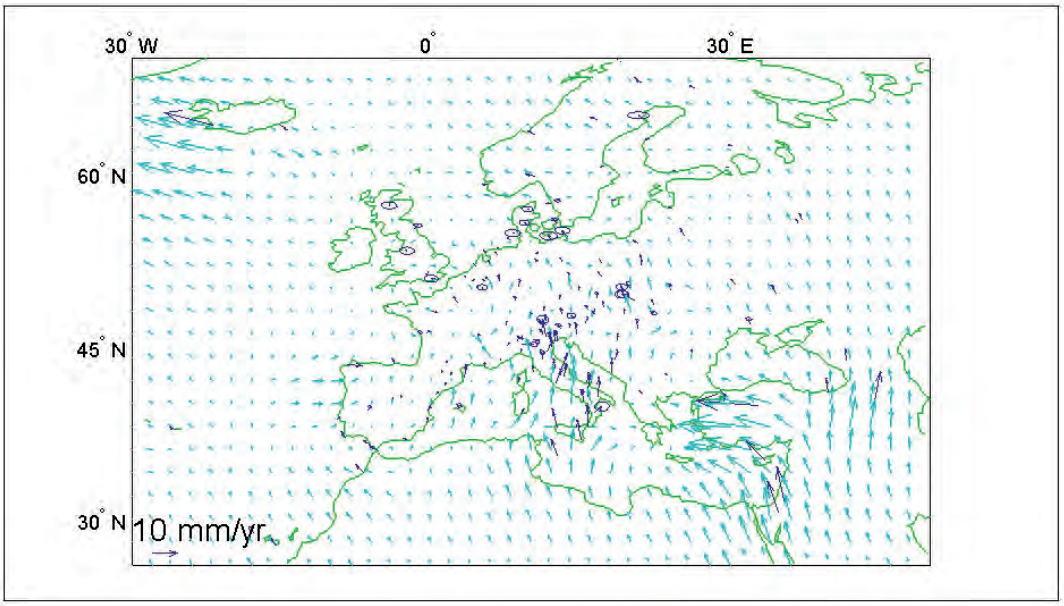

Fig. 4 - Scattered velocities of permanent GPS stations with three or more years of data, after subtraction of the velocity predicted by the model Nuvel1A NNR in terms of rigid rotations about an Eurasian Euler pole. Error ellipses are at 1 σ. Also shown the interpolation, by weighted least squares collocation, of the scattered velocities to a regular grid of 2-degree spacing. Large values of the velocities are visible for the station REYK, in the portion of Iceland belonging to the American plate. The convergence of the African plate with the reference Eurasian plate is visible as a decreasing velocity field northwards. Further east, the counterclockwise motion of Turkey and the convergence of the Arabian plate with Eurasian along the Caucasus appear well defined by the data. Numerical values of the velocities are tabulated in Table 2.

derivatives of the covariance function:

$$\begin{bmatrix} v_{n.n} & v_{n,e} \\ v_{e,n} & v_{e,e} \end{bmatrix}_P = \sum_s \begin{bmatrix} \frac{\partial C}{\partial n} & \frac{\partial C}{\partial e} \\ \frac{\partial C}{\partial n} & \frac{\partial C}{\partial e} \end{bmatrix}_{P,s} \sum_{s'} \left[C\left(d_{s,s'}\right) + w_{ss'} \right]^{-1} \cdot \begin{bmatrix} v_n \\ v_e \end{bmatrix}_{s'} \quad s,s' = station\ indeces \tag{15}$$

The strain-rate matrix is the symmetric part of the matrix described by Eq. (15). The antisymmetric part represents a rigid rotation, and hence gives no contribution to the strain rate. It should be noted that because the covariance function tends to zero as the inverse square of the distance, for values of the distance larger compared to the scale distance, the derivative tends also to zero. Consequently, when interpolating at points with a distance from the data points larger than the scale distance, the collocation algorithm will tend to return a zero strain rate.

Diagonalization of the strain-rate matrix yields the two eigenvectors and the azimuth of the largest:

Table 2 - Horizontal velocities of European permanent GPS stations, with their estimated error ellipses, after subtraction of the rigid rotation velocity about the Eurasian Eulerian pole, as estimated in the Nuvel1A NNR Model (De Mets *et al.*, 1994).

E Lon (°)	N Lat (°)	v_N (mm/yr)	v_E (mm/yr)	min axis (mm/yr)	maj axis (mm/yr)	Az (deg)	site	DOMES
13.51	46.55	0.54	1.23	0.76	1.03	88.38	ACOM	00000M000
-8.40	43.36	5.56	-0.27	0.03	0.04	93.66	ACOR	13434M001
12.17	46.53	-3.12	0.67	0.75	1.01	91.22	AFAL	00000M000
8.76	41.93	0.09	1.27	0.03	0.03	87.89	AJAC	10077M005
-0.48	38.34	0.36	1.56	0.03	0.03	92.77	ALAC	13433M001
-2.46	36.85	-1.07	0.42	0.04	0.05	101.74	ALME	13437M001
32.76	39.89	-24.41	1.35	0.03	0.04	82.45	ANKR	20805M002A
32.76	39.89	-24.47	1.38	0.03	0.04	82.38	ANKR	20805M002C
13.35	42.37	0.61	4.02	0.04	0.05	87.93	AQUI	12757M001B
11.53	45.87	-1.52	5.67	0.25	0.33	90.58	ASIA	12714M001
1.40	41.60	-0.02	0.86	0.03	0.04	84.74	BELL	13431M001
21.04	52.48	-0.36	1.67	0.02	0.03	91.21	BOGI	12207M003
21.04	52.48	-0.36	1.67	0.02	0.02	91.26	BOGO	12207M002A
17.07	52.28	-0.90	0.91	0.02	0.03	91.59	BOR1	12205M002A
6.75	53.56	-0.38	-0.15	0.03	0.05	88.39	BORK	14268M001
11.11	44.12	-0.26	1.33	0.13	0.17	90.02	BRAS	00000M000
10.23	45.56	1.55	-0.58	0.13	0.17	88.95	BRIX	12762M001
-4.50	48.38	0.42	0.36	0.02	0.03	90.96	BRST	10004M004
4.36	50.80	-0.73	-0.36	0.01	0.02	87.85	BRUS	13101M004
26.13	44.46	-0.05	0.58	0.02	0.03	87.36	BUCU	11401M001
12.50	55.74	-0.72	0.94	0.11	0.16	91.27	BUDP	10101M003
19.06	47.48	1.62	-6.18	5.62	7.83	86.15	BUTE	11209M001
11.34	46.50	-2.17	3.07	0.04	0.05	88.74	BZRG	12751M001A
-6.34	39.48	0.61	0.86	0.08	0.09	94.66	CACE	13447M001
8.97	39.14	1.12	1.63	0.02	0.02	94.19	CAGL	12725M003A
8.97	39.14	1.12	1.63	0.02	0.03	94.11	CAGZ	12725M004
13.12	43.11	1.89	4.84	0.03	0.04	88.20	CAME	12754M001
-3.80	43.47	-0.30	1.45	0.04	0.05	94.68	CANT	13438M001
-9.42	38.69	0.83	0.46	0.02	0.03	97.86	CASC	13909S001
12.58	45.48	-0.46	3.22	0.07	0.09	89.77	CAVA	00000M000A
-5.31	35.90	-3.37	1.71	0.08	0.09	97.87	CEUT	13449M001
-0.41	46.13	0.64	0.73	0.04	0.05	92.90	CHIZ	10020M001
9.10	45.80	-0.25	-0.64	0.06	0.08	87.57	COMO	12761M001
16.31	39.20	3.14	2.19	0.33	0.43	81.47	COSE	00000M000
3.32	42.32	0.81	4.24	0.04	0.05	90.76	CREU	13432M001A
-2.64	53.34	0.72	-0.31	0.25	0.35	90.32	DARE	13208S001
4.39	51.99	-0.60	0.48	0.01	0.02	87.44	DELF	13502M004
3.40	50.93	-0.12	0.57	0.01	0.02	88.29	DENT	13112M001
4.60	50.09	-0.28	0.09	0.01	0.02	88.88	DOUR	13113M001
35.39	31.59	-2.82	11.33	0.05	0.07	68.23	DRAG	20710S001
13.73	51.03	0.00	0.97	0.05	0.07	90.11	DRES	14108M001A

Table 2 - continued.

18.11	42.65	-0.15	4.98	0.04	0.06	83.84	DUBR	11901M001
0.49	40.82	0.57	0.64	0.02	0.02	93.64	EBRE	13410M001
5.68	50.76	-0.68	0.62	0.03	0.04	89.25	EIJS	13533M001A
10.21	42.75	-0.23	1.79	0.04	0.05	87.53	ELBA	12721M002
0.98	42.69	0.26	0.54	0.03	0.04	91.75	ESCO	13435M001
6.76	50.67	0.00	1.60	0.04	0.05	89.08	EUSK	14258M003A
20.32	49.03	-4.87	1.76	0.26	0.37	87.39	GANP	11515M001
8.92	44.42	0.31	1.07	0.02	0.02	90.50	GENO	12712M002
30.50	50.36	-1.55	1.60	0.02	0.03	90.52	GLSV	12356M001
14.79	49.91	0.14	0.84	0.01	0.02	88.14	GOPE	11502M002
6.92	43.75	0.12	0.41	0.00	0.00	90.00	GRAS	10002M006
15.49	47.07	0.54	1.69	0.00	0.00	90.00	GRAZ	11001M002A
14.54	46.05	-0.39	3.40	0.07	0.10	86.84	GSR1	14501M001
7.89	54.17	-0.87	0.71	0.02	0.03	89.67	HELG	14264M001
0.33	50.87	-1.41	-0.11	0.25	0.35	88.42	HERT	13212M010
11.39	47.31	0.27	1.87	0.02	0.03	89.80	HFLK	11006S003A
10.48	53.05	0.60	0.11	0.03	0.04	90.16	HOBU	14202M003
8.29	54.76	-0.61	0.16	0.24	0.36	90.03	HOER	14284M001
-15.20	64.27	2.65	-2.01	0.03	0.04	83.45	HOFN	10204M002A
7.64	45.02	0.49	0.95	0.03	0.03	88.61	IENG	12724S001
12.51	41.83	1.84	4.33	0.08	0.10	88.47	INGR	00000M000
-4.22	57.49	-0.10	-1.11	0.24	0.35	89.00	INVE	13221S001
29.02	41.10	2.20	-1.82	0.03	0.03	82.72	ISTA	20807M001
30.10	62.39	-0.93	0.12	0.02	0.02	97.85	JOEN	10512M001
21.03	52.10	0.21	1.43	0.00	0.00	90.00	JOZ2	12204M002
8.41	49.01	-0.29	0.95	0.05	0.07	89.47	KARL	14216M001A
19.04	50.25	0.52	-2.99	0.22	0.31	87.25	KATO	12219S001
-50.94	66.99	-17.54	-2.58	0.05	0.06	85.20	KELY	43005M001A
21.06	67.88	-1.89	0.54	0.01	0.02	96.18	KIR0	10422M001
20.97	67.86	-2.32	1.61	0.02	0.02	95.64	KIRU	10403M002
8.73	50.22	0.45	2.12	0.04	0.06	88.69	KLOP	14214M002A
5.81	52.18	-0.57	0.98	0.01	0.02	86.61	KOSG	13504M003A
19.92	50.07	-0.83	1.37	0.11	0.16	87.58	KRAW	12218M001
-8.67	37.10	-1.48	1.56	0.07	0.08	163.19	LAGO	13903M001
20.67	53.89	-1.60	1.08	0.02	0.03	91.64	LAMA	12209M001A
12.61	35.50	-2.42	5.45	0.02	0.03	89.54	LAMP	12706M002
9.41	45.86	0.09	4.93	1.54	1.98	91.05	LEC1	12768M001
14.28	48.31	-1.89	0.18	0.33	0.46	87.99	LINZ	11033S001
1.97	42.48	0.05	0.90	0.03	0.04	93.41	LLIV	13436M001
-17.89	28.76	-0.92	1.59	0.13	0.14	129.68	LPAL	81701M001
-1.22	46.16	0.28	0.12	0.09	0.12	94.26	LROC	10023M001
2.62	39.55	0.66	1.15	0.13	0.16	90.60	MALL	13444M001
0.16	48.02	1.36	-0.42	0.02	0.03	89.99	MANS	10091M001
17.26	60.60	-1.27	-0.22	0.01	0.02	91.96	MAR6	10405M002

Table 2 - continued.

15.69	40.00	-2.79	-2.18	0.43	0.55	80.03	MARA	00000M000
5.35	43.28	-0.08	0.89	0.03	0.05	90.00	MARS	10073M008
-15.63	27.76	-1.87	2.25	0.03	0.03	128.43	MAS1	31303M002
16.70	40.65	0.32	6.30	0.02	0.02	61.45	MATE	12734M008A
13.44	45.92	-0.96	2.84	1.00	1.32	78.48	MDEA	12765M001
37.22	56.03	-1.00	1.60	0.03	0.04	94.75	MDVO	12309M002A
11.65	44.52	1.78	3.08	0.01	0.01	89.59	MEDI	12711M003
11.16	46.67	-0.13	0.09	0.00	0.00	90.00	MERA	00000M000A
24.40	60.22	-0.62	0.01	0.01	0.02	97.27	METS	10503S011
31.97	46.97	-0.61	1.42	0.12	0.16	87.18	MIKL	12335M001
12.58	38.01	-1.87	5.88	0.06	0.07	86.34	MILO	00000M000
2.59	48.84	-1.26	1.50	0.03	0.04	90.66	MLVL	10092M001
17.27	48.37	-0.33	1.82	0.02	0.03	89.62	MOPI	11507M001
-1.69	55.21	1.34	1.06	0.13	0.19	89.63	MORP	13299S001
12.99	46.24	-0.97	2.74	0.66	0.88	86.98	MPRA	12764M001
11.65	44.52	4.14	-5.24	4.49	6.08	90.61	MSEL	12711M008
-5.54	50.10	-2.23	5.62	0.91	1.28	91.66	NEWL	13273M103
33.40	35.14	-7.08	6.33	0.02	0.02	67.93	NICO	14302M001
14.99	36.88	-1.41	6.46	0.04	0.05	80.16	NOT1	12717M004
14.99	36.88	-1.40	6.44	0.04	0.05	80.50	NOTO	12717M003A
8.61	45.45	0.41	1.41	0.05	0.07	88.13	NOVA	00000M000
-0.34	51.42	-0.59	-0.86	0.04	0.06	89.58	NPLD	13234M003
44.50	40.23	2.23	10.07	0.04	0.04	84.83	NSSP	12312M001
11.87	78.93	-2.04	-0.54	0.02	0.03	89.09	NYA1	10317M003
22.14	47.84	0.49	0.18	0.13	0.18	87.42	NYIR	11208M001
11.28	48.09	0.05	1.24	0.03	0.04	89.14	OBER	14208M001A
11.28	48.08	0.05	1.24	0.03	0.04	89.13	OBET	14208M004
11.93	57.40	-1.39	-0.04	0.01	0.02	89.63	ONSA	10402M004
20.79	41.13	0.92	-0.62	0.04	0.05	79.03	ORID	15601M001
20.67	46.56	-0.20	2.78	0.08	0.11	86.33	OROS	11207M001A
18.68	45.56	0.02	1.92	0.03	0.04	86.17	OSJE	11902M001
10.37	59.74	-3.38	0.68	0.03	0.05	90.33	OSLS	10307M001
11.90	45.41	-0.10	3.05	0.03	0.04	88.04	PADO	12750S001
11.46	47.21	-0.03	1.39	0.05	0.07	88.29	PATK	11029S001
9.14	45.20	4.43	-0.33	0.16	0.21	87.61	PAVI	00000M000B
-25.66	37.75	-1.96	0.37	0.07	0.08	170.93	PDEL	31906M004
19.28	47.79	0.28	1.45	0.01	0.02	88.94	PENC	11206M006A
9.78	47.52	0.95	1.36	0.04	0.05	87.74	PFAN	11005S002A
-4.11	50.44	-4.17	-3.05	1.80	2.48	91.87	PLYM	13229S001
34.54	49.60	-1.51	2.40	0.06	0.08	88.58	POLV	12336M001
13.07	52.38	-0.65	0.90	0.00	0.00	90.00	POTS	14106M003
11.10	43.89	0.59	2.57	0.05	0.06	90.36	PRAT	12760M001
10.46	52.30	0.10	0.61	0.06	0.08	88.25	PTBB	14234M001A
13.84	44.89	0.11	3.72	0.60	0.79	85.98	PULA	11903S001

Table 2 - continued.

-46.05	60.72	-19.55	0.79	0.12	0.18	92.26	QAQ1	43007M001
-6.85	34.00	-2.75	2.42	0.06	0.06	107.55	RABT	35001M002
34.76	30.60	-4.10	10.48	0.03	0.03	73.54	RAMO	20703S001
5.14	50.00	-0.36	0.38	0.19	0.27	89.29	REDU	13102M001
-21.96	64.14	-19.03	4.49	0.02	0.02	68.95	REYK	10202M001
24.06	56.95	-1.09	0.55	0.02	0.02	93.36	RIGA	12302M002
11.04	45.89	-0.40	0.09	1.01	1.33	92.32	ROVE	00000M000
11.78	45.09	-2.78	0.59	1.59	2.09	91.59	ROVI	12769M001
14.34	47.52	-1.34	0.41	0.18	0.24	86.50	RTMN	00000M000
13.64	54.51	-2.16	2.03	0.24	0.35	89.01	SASS	14281M001
13.11	47.80	-0.43	1.57	0.06	0.08	88.82	SBGZ	11031S001A
12.29	45.23	-1.76	2.19	0.07	0.09	89.72	SFEL	00000M000A
-6.21	36.46	-2.46	1.37	0.02	0.02	105.75	SFER	13402M004
4.68	45.88	0.21	0.44	0.05	0.06	88.99	SJDV	10090M001A
4.68	45.88	0.20	0.44	0.05	0.06	89.01	SJDV	10090M001C
21.05	64.88	-1.12	0.52	0.24	0.37	89.57	SKE0	10426M001
9.56	55.64	-0.99	0.17	0.18	0.27	90.06	SMID	10114M001
26.39	67.42	-1.59	0.52	0.02	0.02	98.84	SODA	10513M001
23.39	42.56	0.80	-0.31	0.02	0.02	86.07	SOFI	11101M002
12.89	57.72	-0.98	-0.39	0.09	0.14	90.40	SPT0	10425M001
18.41	43.87	0.98	2.81	0.06	0.07	83.58	SRJV	11801S001A
5.60	59.02	-1.40	-0.16	0.03	0.05	86.71	STAS	10330M001
15.63	48.20	-0.48	0.92	0.05	0.07	94.26	STPO	00000M000
9.74	56.84	-0.50	0.18	0.18	0.26	90.04	SULD	10113M001
24.01	49.84	-0.52	1.86	0.06	0.09	86.66	SULP	12366M001
29.78	60.53	-0.45	-0.08	0.03	0.03	89.23	SVTL	12350M001
17.28	40.53	0.56	12.42	1.60	1.97	83.31	TARS	12773S001
5.22	53.36	0.69	-0.75	0.03	0.04	88.74	TERS	13534M001A
15.65	38.11	-0.04	6.44	0.09	0.11	82.04	TGRC	00000M000B
-68.83	76.54	-14.88	-5.78	0.15	0.17	108.04	THU3	43001M002
15.72	40.60	0.30	7.64	0.12	0.14	84.37	TITO	00000M000
1.48	43.56	0.23	0.37	0.03	0.04	89.85	TLSE	10003M009
39.78	40.99	-0.77	4.84	0.03	0.04	81.14	TRAB	20808M001
10.32	63.37	-1.96	0.95	0.03	0.05	88.18	TRDS	10331M001
11.12	46.07	-0.63	1.03	0.09	0.12	89.14	TREN	12753M001B
13.76	45.71	-1.76	3.52	0.72	0.95	88.08	TRIE	00000M000
18.94	69.66	-1.29	1.68	0.02	0.03	93.01	TRO1	10302M006
16.59	49.21	-0.15	1.45	0.06	0.08	86.20	TUBO	11503M001
24.07	35.53	-20.35	-23.67	4.35	5.12	84.24	TUC2	12617M003
12.36	43.12	-0.43	2.70	0.04	0.05	89.00	UNPG	12752M001A
11.88	45.41	-0.06	3.07	0.03	0.04	88.10	UPAD	12750M002A
21.77	62.96	-1.11	-0.13	0.01	0.02	94.34	VAAS	10511M001
-0.34	39.48	1.05	0.98	0.06	0.07	96.20	VALE	13439M001
31.03	70.34	-1.41	0.12	0.04	0.05	99.14	VARS	10322M002

Table 2 - continued.

12.33	45.44	-0.11	2.88	0.03	0.03	88.73	VENE	12741M001A
16.56	64.70	-2.14	0.46	0.01	0.02	93.10	VIL0	10424M001
13.85	46.61	-0.02	1.12	0.04	0.06	92.93	VILH	00000M000
-3.95	40.44	0.47	0.15	0.00	0.00	90.00	VILL	13406M001
18.37	57.65	-1.05	-0.01	0.01	0.02	91.52	VIS0	10423M001
25.30	54.65	-1.13	1.96	0.05	0.07	95.00	VLNS	10801M001
15.27	40.23	-22.59	-9.65	0.11	0.13	84.29	VLUC	00000M000A
11.91	45.38	-0.44	2.73	0.07	0.09	89.54	VOLT	00000M000A
5.25	50.69	-0.09	0.11	0.02	0.03	89.41	WARE	13114M001A
12.10	54.17	-1.45	1.61	0.28	0.41	89.65	WARN	14277M002
12.88	49.14	0.11	0.94	0.02	0.02	92.12	WETT	14201M009
16.37	48.22	-0.56	-1.30	0.07	0.09	94.25	WIEN	00000M000A
17.06	51.11	-1.41	1.13	0.01	0.02	89.30	WROC	12217M001
6.60	52.91	-0.68	0.85	0.02	0.02	90.37	WSRT	13506M005
12.88	49.14	0.01	0.99	0.02	0.02	92.04	WTZR	14201M010A
-3.09	40.52	0.19	0.66	0.03	0.04	96.24	YEBE	13420M001
41.57	43.79	-0.08	3.73	0.02	0.03	82.44	ZECK	12351M001
7.47	46.88	0.29	0.85	0.00	0.00	90.00	ZIMM	14001M004A
7.47	46.88	0.29	0.85	0.00	0.00	90.00	ZIMM	14001M004B
7.47	46.88	0.29	0.85	0.00	0.00	90.00	ZIMM	14001M004C
12.97	46.56	-0.98	1.01	0.12	0.16	89.88	ZOUF	12763M001
36.76	55.70	-0.74	1.07	0.02	0.03	93.91	ZWEN	12330M001
19.21	49.69	-0.49	1.77	0.21	0.29	87.39	ZYWI	12220S001

$$\dot{\varepsilon}_1 = \frac{v_{n.n} + v_{e,e}}{2} + \sqrt{\left(\frac{v_{e,e} - v_{n,n}}{2}\right)^2 + \left(\frac{v_{e,n} + v_{n,e}}{2}\right)^2}$$

$$\dot{\varepsilon}_2 = \frac{v_{n,n} + v_{e,e}}{2} + \sqrt{\left(\frac{v_{e,e} - v_{n,n}}{2}\right)^2 + \left(\frac{v_{e,n} + v_{n,e}}{2}\right)^2} \qquad (16)$$

$$\sin 2\theta = \frac{v_{n,n} + v_{n,e}}{\dot{\varepsilon}_2 - \dot{\varepsilon}_1}; \cos 2\theta \frac{v_{e,e} + v_{n,n}}{\dot{\varepsilon}_1 - \dot{\varepsilon}_2}$$

A positive strain-rate implies an increasing relative velocity between two nearby points, and hence an extension. Likewise, a negative eigenvalue indicates compression. Areas subject to expansion or contraction are also possible. In such case, the two eigenvalues are both respectively negative or positive. The maximum shear strain is finally given by the difference of the absolute values of the two eigenvalues. We shall however adopt the convention that compression has a positive strain rate and extension a negative strain-rate later.

The covariance of the scattered velocities at the data points maps, linearly, into a covariance of the strain rate tensor in geographical coordinates. Linearization of Eq. (16) relative to small uncertainties in the normal and shear components of the strain rate yields the required uncertainties in the principal

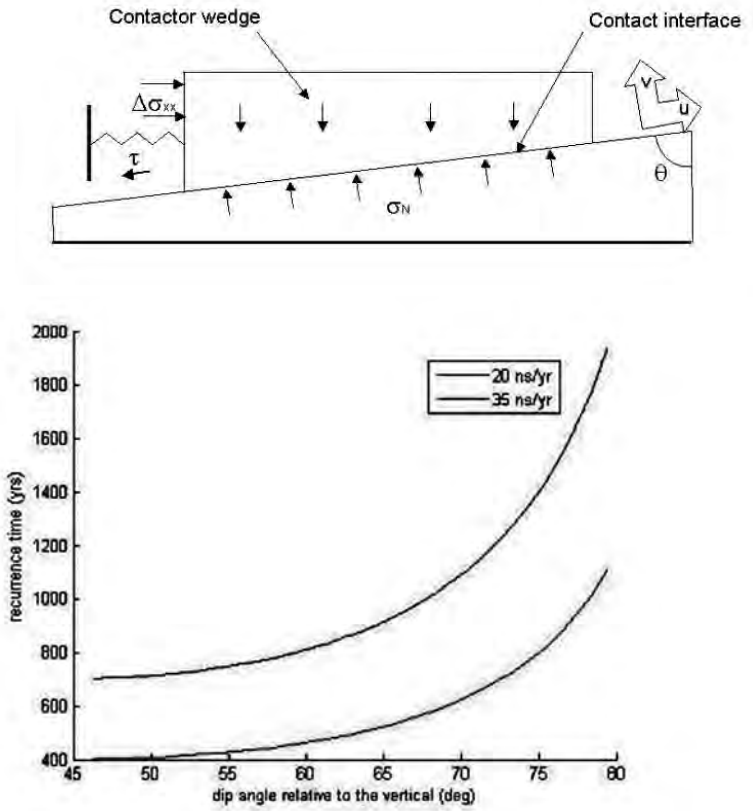

Fig. 5 - Idealized slider block model.

strain rates and in the azimuth. Hence, the collocation algorithm enables principal values of the strain rate and the azimuth to be interpolated rigorously, and the uncertainties to be estimated in a formal sense from the nominal values and full covariance of the input, scattered velocities.

The scattered velocities are shown in Fig. 4, together with their interpolation at a regular grid of 2 degree spacing, to obtain a general look of the estimated European kinematics inferred from GPS data.

5. Constraining an idealized earthquake cycle with geodetic data

The surface strain which is implied by the geodetic data, possibly in conjunction with InSAR data, is considered of great interest in earthquake research and mitigation of the earthquake hazard. It is, therefore, important to develop simple models to understand in detail how one can fit the geodetic information into a picture which already contains seismological and structural data. The simplest model is that of a slider block (Fig. 5). The surface of contact dips at an angle $\delta = 90° - \theta$ relative to the horizontal, and the two blocks are subject to a horizontal deviatoric stress $\Delta\sigma_{xx}$. In the following subsections we review the static and dynamic information which can be predicted with such a simple model.

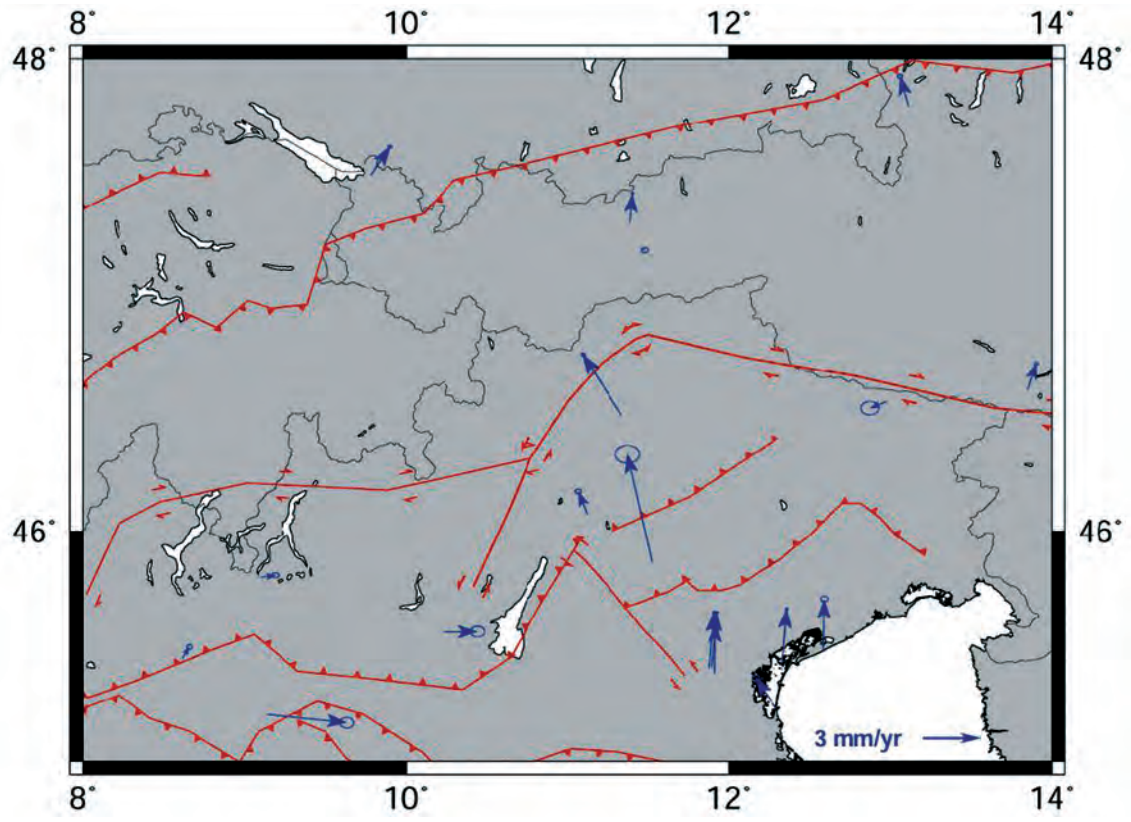

Fig. 6 - Velocities of permanent GPS stations and fault geometries in the central eastern Alps. Error ellipses are 1σ confidence.

5.1. Static analysis

We intend to determine here the maximum value of the horizontal deviatoric stress at which the sliding instability occurs along the fault plane, using the classical theory of Anderson, as described in Turcotte and Schubert (2002). To this purpose (see Fig. 5), we introduce the normal σ_n and tangential τ stresses, relative to the fault plane, and the angle of the fault plane relative to the vertical $\theta = 90° - \delta$. Then:

$$\sigma_n = phg - p_w + \frac{\Delta\sigma_{xx}}{2}(1+\cos 2\theta)$$
$$\tau = \pm\frac{\Delta\sigma_{xx}}{2}\sin 2\theta \qquad (17)$$

where p_w is the pore pressure that opposes to the lithostatic load. We define the onset of the instability in terms of the Amonton law, i.e. when the tangential stress equals the normal stress times the coefficient of static friction f_s. This criterion is legitimate for temperatures low enough for the concept of friction to be applied. According to Amonton's law instability occurs when

$$\tau = f_s \sigma_n \Rightarrow \Delta\sigma_{xx} = \frac{2 f_s \left(\rho g h - p_w\right)}{\pm \sin 2\theta - f_x \left(1 + \cos 2\theta\right)} \tag{18}$$

where the upper sign refers to thrust faults and the lower sign to normal faults.

To compute the displacement along the fault, say in the u direction, we assume that the deformation at the fault surface is elastic, with a shear modulus μ. We further assume that the rupture area is a square of side $A^{1/2}$. This enables us to relate the tangential stress to the displacement in terms of the Hooke law:

$$\tau = \frac{\mu u}{2\sqrt{A}}, \tag{19}$$

It follows that the instability takes place when the displacement along the fault has reached a limit value:

$$u_s = \frac{2\sqrt{A} f_s \sigma_n}{\mu} = \frac{\sqrt{A} \Delta\sigma_{xx} \sin 2\theta}{\mu}. \tag{20}$$

5.2. Dynamical analysis

In this section, we attempt to model the motion of the slider from the epoch t=0 at which the sliding instability occurs and the epoch at which the slider stops. We assume that the acceleration of the slider along the fault plane is caused by the algebraic sum of the restoring elastic stress and a constant dynamic friction, again proportional to the normal critical stress, *i.e*. the one corresponding to the maximum deviatoric stress. The equation of motion is then

$$\rho A^{3/2} \frac{d^2 u}{dt^2} + \frac{\mu A^{1/2} u}{2} = f_d \sigma_n A, \tag{21}$$

where f_d is the coefficient of dynamic friction. The solution of this equation of motion satisfying a first boundary condition of zero velocity at t = 0 is of the type:

$$u(t) = a \cos \omega t + b, \quad with \quad \omega = \sqrt{\frac{\mu}{2\rho A}}; \quad b = \frac{2 f_d \sigma_n \sqrt{A}}{\mu}. \tag{22}$$

The second boundary condition $u(0) = u_s$ defines the amplitude of the elastic rebound:

$$a = \frac{2\left(f_s - f_d\right)\sigma_n \sqrt{A}}{\mu}. \tag{23}$$

The rebound lasts from t = 0 to the time at which the velocity is again zero, that is:

$$t = \pi \sqrt{\frac{2\rho A}{\mu}} \tag{24}$$

The corresponding displacement is:

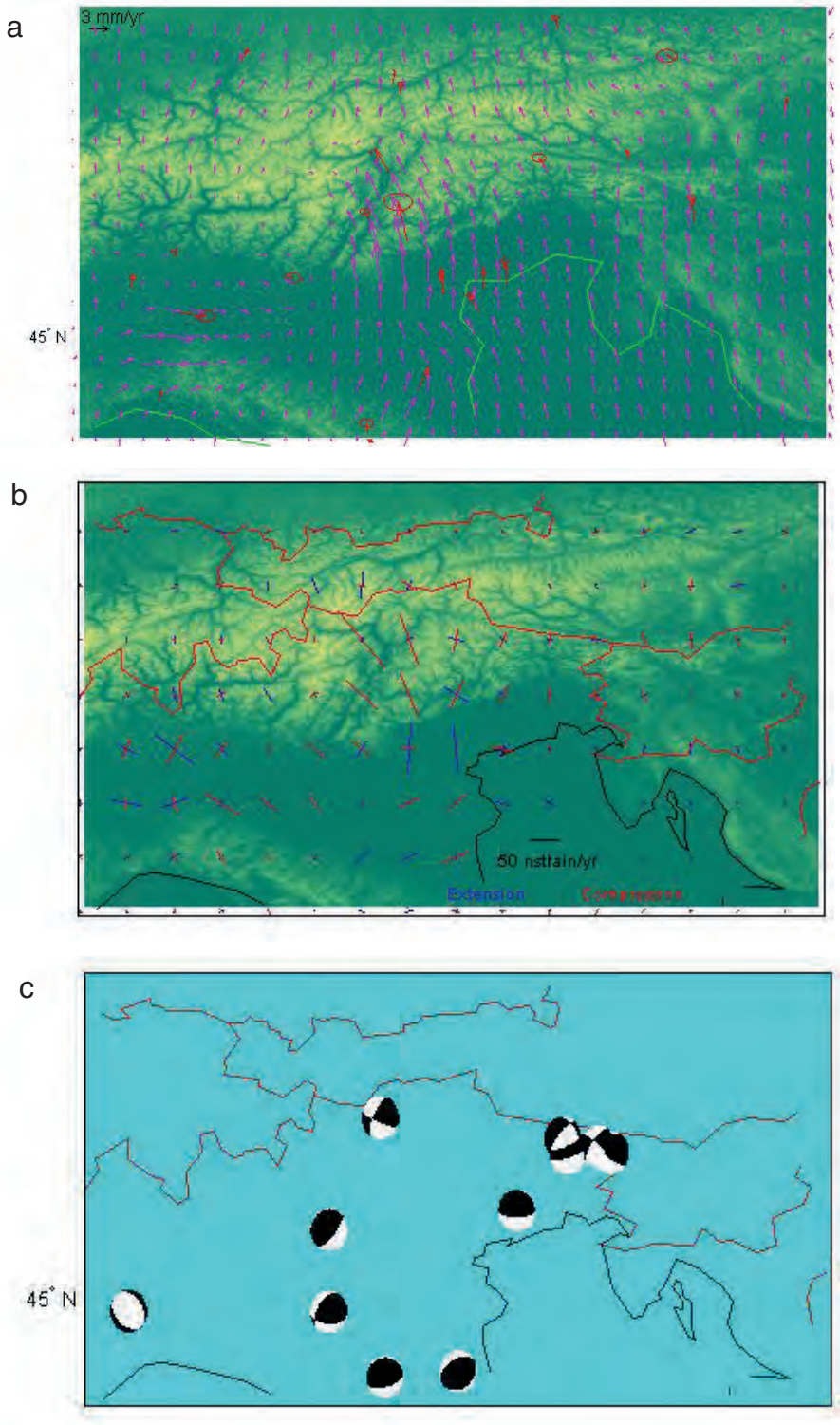

Fig. 7 - Velocity field (a), strain rate (b) and fault plane solutions in the past 30 years (c) in Friuli, inferred from geodetic data. Fault plane solutions detailed in Table 3.

Table 3 - Fault plane solutions of the largest Eastern Alps earthquakes in the last 30 years (sources: http://www.ingv.it/seismoglo/RCMT/; http://www.seismology.harvard.edu/projects/CMT/). Epicentral coordinates in degrees, strike dip and slip angles of the two planes in degrees, Seismic moment basis and exponent in units of 10^{-7} Nm.

lon	lat	strike1	dip1	slip1	strike2	dip2	slip2	M_0	exp	epoch
13.17	46.33	284	18	119	74	74	81	6.33	25	050676
12.63	45.8	298	24	117	89	69	79	1.41	24	091677
17.33	44.86	152	55	-169	55	81	-36	3.9	24	081381
10.62	44.86	217	53	47	94	54	132	1.46	24	101596
13.50	46.39	218	67	-4	309	87	-157	3.5	24	041298
12.00	44.31	55	39	83	245	51	96	4.76	23	051000
8.48	44.87	130	44	-97	321	46	-83	2.75	23	082100
11.17	46.66	210	69	16	114	75	159	1.57	23	071701
11.22	44.26	264	31	98	74	60	85	1.026	24	091403
13.12	46.47	327	38	-158	219	77	-54	11.96	22	021402
13.63	46.34	237	43	27	126	72	129	8.73	23	071204
10.62	45.62	246	24	113	42	68	80	4.26	23	112404

$$\Delta u = 2u_s\left(1-\frac{f_d}{f_s}\right), \tag{25}$$

This corresponds to a scalar seismic moment:

$$M_0 = \mu A \Delta u, \tag{26}$$

and a shear stress drop:

$$\Delta\tau = \frac{\mu\Delta u}{2\sqrt{A}} = \frac{M_0}{2A^{3/2}}. \tag{27}$$

The shear stress remaining in the rocks after the slip event has occurred is the difference between the total available shear stress [Eq. (19)] corresponding to a limit displacement given by Eq. (20), and the shear stress drop [Eq. (27)]:

$$\tau^{(0)} = \tau\left(u_s\right) - \Delta\tau = \frac{\mu u_s A - M_0}{2A^{3/2}}. \tag{28}$$

This residual shear stress on the fault plane corresponds to a residual deviatoric stress in the horizontal direction:

$$\sigma_{xx}^{(0)} = \frac{2\tau^{(0)}}{\pm\sin 2\theta} = \frac{2f_s\sigma_n\left(2\frac{f_d}{f_s}-1\right)}{\pm\sin 2\theta}. \tag{29}$$

5.3. Interseismic analysis

In a plane-stress approximation the critical deviatoric stress $\Delta\sigma_{xx}$ in an area subject to a uniform strain rate and preloaded by a deviatoric stress $\sigma_{xx}^{(0)}$, for example a remnant of a previous seismic event, is obtained after a time Δt counted from the last epoch of onset of the instability:

$$\Delta\sigma_{xx} = \frac{E\dot{\varepsilon}_{xx}\Delta t}{1-\nu^2} + \sigma_{xx}^{(0)}, \tag{30}$$

E and ν are the Young modulus and Poisson ratio respectively, and μ= E/[2(1+ν)]. The process of stress accumulation on a fault plane may involve a number of random, smaller events which drain from the strain rate and hence lengthen the time required to reach the critical deviatoric stress. For example, if we are interested in the time required to reach the deviatoric stress of an earthquake of magnitude larger than 6, then we have to subtract from the total, 'steady state' geodetic strain rate the average strain rate which is drained by earthquakes of magnitude smaller or equal to 6 in the same area and time interval. The remaining strain rate should of course account for the main shocks and the fore/after shocks as well. This average strain rate can be estimated by the Kostrov formula by considering the sum of the scalar moments of the earthquakes of magnitude not larger than 6 in the fracture area A, over a reference interval Δt:

$$\dot{\varepsilon}_{xx,m\le 6} = \frac{\sum_{m\le 6} M_0}{2\mu A h \Delta t} \tag{31}$$

Hence, the strain rate to be considered in Eq. (30) is the difference between the geodetic strain rate inferred from GPS and the Kostrov strain rate defined by Eq. (31).

The residual deviatoric stress leftover by the previous sliding instability depends on a dip angle, seismic moment, rupture area, dynamic friction, hypocentral depth and other parameters which need not to be equal to that of the current earthquake. We will examine here the case in which the only parameter allowed to differ from one earthquake to the next is the dip angle. Under this assumption, we have [see Eq. (29)] that the last earthquake took place at a dip angle 90°-$\theta^{(0)}$ and left a deviatoric stress:

$$\sigma_{xx}^{(0)} = \frac{\mu u_s^{(0)} A^{(0)} - M_0^{(0)}}{\pm {A^{(0)}}^{3/2} \sin 2\theta^{(0)}}. \tag{32}$$

It follows from Eq. (30) that the deviatoric stress to be built from one event to the next is

$$\Delta\sigma_{xx} - \sigma_{xx}^{(0)} = \frac{\mu u_s A}{\pm A^{3/2} \sin 2\theta} - \frac{\mu u_s^{(0)} A^{(0)} - M_0^{(0)}}{\pm {A^{(0)}}^{3/2} \sin 2\theta^{(0)}}. \tag{33}$$

The repeat time is obtained from Eqs. (30) and (33), taking into account Eq. (31) for computing the effective strain rate.

We address the recurrence of consecutive instabilities along the same plane, that is $\theta = \theta^{(0)}$. The angle of minimum stress satisfies the condition $\tan 2\theta = \pm 1/f_s$. It follows that the estimated

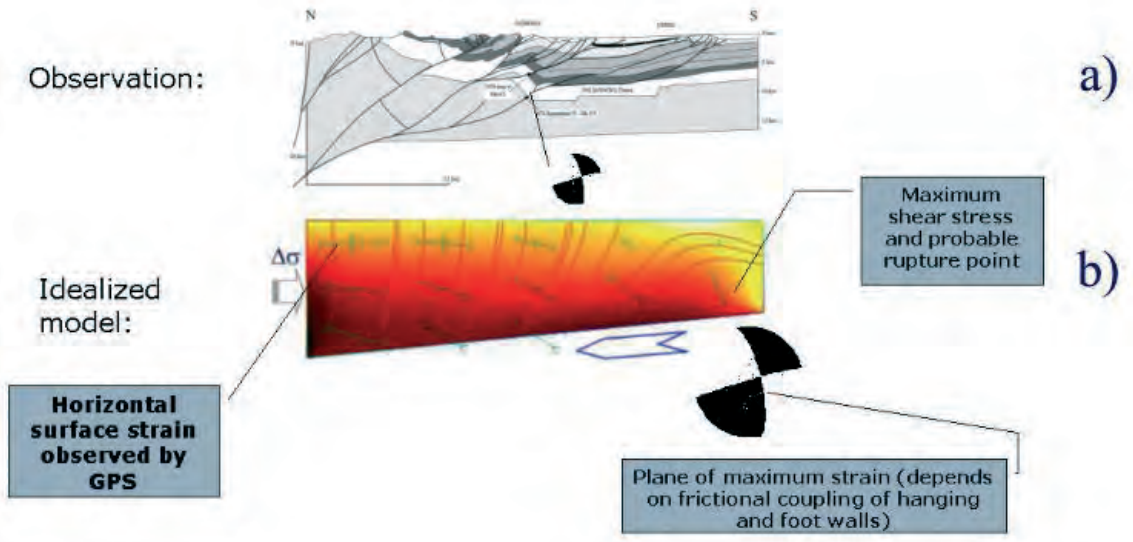

Fig. 8 - Structural geology and a sliding block model: (a)vertical profile, from Galadini *et al*. (2005); (b) sliding wedge geometry highlighting the deviatoric stress, an elastic shear stress acting on the sliding plane, the lithostatic body force and the fault plane solution of the May 6, 1976 event given in Table 3. Note that the eigenvector is nearly horizontal where the deviatoric stress is applied, and turns to high dip angle close to the sliding surface, in agreement with the fault plane solution.

recurrence time of two identical slip events along the same plane is:

$$\Delta t = \frac{M_0}{\pm A^{3/2} \sin 2\theta} \frac{1-\upsilon^2}{E\dot{\varepsilon}} \geq \pm \frac{M_0 \sqrt{1+f_s^2}}{A^{3/2}} \frac{1-\upsilon^2}{E\dot{\varepsilon}}. \tag{34}$$

Hence, the recurrence time basically depends on the shear stress drop (27) projected on the horizontal. The strain rate is assumed negative for extension and positive for compression, which ensures a positive accumulation time. This is the same regardless of the compressional/ extensional stress regime, while the deviatoric stress $\Delta\sigma_{xx}$ does depend on the regime. Fig. 5b shows Eq. (34) for two values of the strain rate, 20 and 35 nstrain/yr, which should be typical for Friuli. We have further assumed $M_0 = 6.33\ 10^{18}$ Nm and $A = 325\ 10^6$ m^2, which should be typical for the May 6, 1976 event (Galadini *et al*., 2005). Unfortunately, there is no historical earthquake that may be considered a predecessor of the 1976 event, so that Eq. (34) is not very useful in this case.

One can however extend Eq. (33) to the case in which an event at some location and time leaves a residual stress which is then propagated in space and time according to some mechanism, such as viscoelastic diffusion with respect to some underlying viscous channel. Then, depending on the diffusion coefficient, stress can propagate from one area to the other, and help in activating it.

Fig. 6 describes the fault pattern superimposed on the kinematics in the Friuli area, which comes from the analysis of time series of permanent GPS stations. Fig. 7 represents the velocity field, the strain rate field and the fault plane solutions of the events listed in Table 3. Finally, Fig. 8 gives the

vertical profile of the area activated with the 1976 earthquakes (Galadini *et al*., 2005), the corresponding idealization with the sliding block model and, finally, a finite element simulation showing how the strain direction, depending on the friction on the interface, may dip at a larger angle at depth than at the surface.

6. Conclusion

The analysis of long-time series of displacements of permanent GPS stations yields rigorous velocity data and associated uncertainty, which can be interpolated to a grid of velocities and eigenvectors of the strain rate tensor by least squares collocation, keeping control of the error. Consequently, depending on the local concentration of stations and period of activity it is now possible to monitor surface-strain accumulation with an accuracy on average of the order 10%. We require structural and geophysical data of the same accuracy in seismogenic areas, and a model of stress build-up and release that can make use of these data. As a first attempt, we have used the classical Anderson theory of faulting to develop a simple analytical framework in which the geodetic strain rate is combined with the frictional dynamics of a sliding wedge on an inclined interface. Considering such very crude predictions confronts us with some important questions: to which extent the parameters of the model, such as dip angle of the fault, friction coefficient, rupture area, elastic constants, pore fluid pressure, hypocentral depth… are well constrained? Are there any pairs of event which may be considered one the replica of the other? Do we have any mean to transfer elastic stress aseismically between two neighbouring areas? As the geodetic data keep improving in accuracy and spatial resolution, the importance of seismic profiling and of the measurement of stress in rocks appears crucial in making even simple theoretical models truly useful.

Acknowledgment. This research is supported by the EU Project CERGOP 2 of the 5. Framework Programme, coordinated by dr. Peter Pesec, and by the MIUR PRIN Project 'Ricostruzione del quadro deformativo a breve-medio termine della regione Mediterranea Centrale: implicazioni per una stima deterministica della pericolosità sismica' coordinated by Prof. E. Mantovani. The author gratefully acknowledges the comments of two anonymous Referees.

REFERENCES

Allan D.W.; 1966: *Statistics of atomic frequency standards.* In: Proc. IEEE, pp. 221-330.

Beutler G., Brockmann E., Fankhauser S., Gurtner W., Johnson J., Mervart L., Rothacher M., Schaer S., Springer T. and Weber R.; 2001: *Bernese GPS software version 4.2.* In: Hugentobler U., Schaer S. and Fridez P. (eds), Astronomical Institute of the University of Bern, 418 pp.

Bruyninx C.; 2000: *Overview of the EUREF permanent network and the network coordination activities*. Report on the Symposium of the IAG Subcommission for Europe (EUREF), Tromsø 22-24 June 2000. In: Torres J.A. and Hornik H. (eds), Veröffentlichungen der Bayerischen Kommission für die Internationale Erdmessung der Bayerischen Akademie der Wissenschaften, Astronomisch Geodätische Arbeiten, Heft n. **61**, pp. 24-30.

Caporali A.; 2003: *Average strain rate in the Italian crust inferred from a permanent GPS network I. Statistical analysis of time series of permanent GPS stations.* Geophys. J. Int., **155**, 241-253.

Caporali A., Martin S. and Massironi M.; 2003: *Average strain rate in the Italian crust inferred from a permanent GPS network I. Strain rate vs. Seismicity and Structural Geology.* Geophys. J. Int., **155**, 254-268.

De Mets C., Gordon R.G., Argus D.F. and Stein S.; 1994: *Effect of recent revisions to the geomagnetic reversal time scale on estimates of current plate motions.* Geophys. Res. Lett., **21**, 2191-2194.

Galadini F., Poli M.E. and Zanferrari A.; 2005: *Seismogenic sources potentially responsible for earthquakes of M>=6 in the Eastern Southern Alps (Thiene Udine Sector, NE Italy).* Geophys. J. Int., **161**, 739-762.

Montrasio A. and Sciesia E. (eds); 1994: Proceedings of the Syposium CROP- Alpi Centrali. Quaderni di Geodinamica Alpina e Quaternaria, CNR Milano, **2**, 296 pp.

Transalp Working Group; 2002: *First deep seismic reflection images of the Eastern Alps reveal giant crustal wedges and transcurrent ramps.* Geoph. Res. Letters 29, 101029-101032.

Turcotte D.L. and Schubert G.; 2002: *Geodynamics.* Cambridge University Press, 472 pp.

Corresponding author: Alessandro Caporali
Dipartimento di Geologia, Paleontologia e Geofisica,
Università di Padova
Via Giotto 1, 35137 Padova
phone: 049/8272052; fax: 049/8272070